INAF
ISTITUTO NAZIONALE
DI ASTROFISICA
NATIONAL INSTITUTE
FOR ASTROPHYSICS

Publication Year	2021
Acceptance in OA	2022-06-10T14:02:16Z
Title	Extremely deep 150 MHz source counts from the LoTSS Deep Fields
Authors	Mandal, S., PRANDONI, ISABELLA, Hardcastle, M. J., Shimwell, T. W., Intema, H. T., Tasse, C., van Weeren, R. J., Algera, H., Emig, K. L., Röttgering, H. J. A., Schwarz, D. J., Siewert, T. M., Best, P. N., BONATO, MATTEO, BONDI, MARCO, Jarvis, M. J., Kondapally, R., Leslie, S. K., Mahatma, V. H., Sabater, J., Retana-Montenegro, E., Williams, W. L.
Publisher's version (DOI)	10.1051/0004-6361/202039998
Handle	http://hdl.handle.net/20.500.12386/32271
Journal	ASTRONOMY & ASTROPHYSICS
Volume	648

A&A 648, A5 (2021)
https://doi.org/10.1051/0004-6361/202039998
© ESO 2021

Astronomy & Astrophysics

The LOFAR Two Meter Sky Survey

Special issue

Extremely deep 150 MHz source counts from the LoTSS Deep Fields

S. Mandal[1], I. Prandoni[2], M. J. Hardcastle[3], T. W. Shimwell[1,4], H. T. Intema[1,5], C. Tasse[6,7], R. J. van Weeren[1], H. Algera[1], K. L. Emig[1], H. J. A. Röttgering[1], D. J. Schwarz[8], T. M. Siewert[8], P. N. Best[9], M. Bonato[2,10,11], M. Bondi[2], M. J. Jarvis[12,13], R. Kondapally[9], S. K. Leslie[1], V. H. Mahatma[14], J. Sabater[9,15], E. Retana-Montenegro[16], and W. L. Williams[1]

[1] Leiden Observatory, Leiden University, PO Box 9513, 2300 RA Leiden, The Netherlands
e-mail: mandal@strw.leidenuniv.nl
[2] INAF - IRA, Via P. Gobetti 101, 40129 Bologna, Italy
e-mail: prandoni@ira.inaf.it
[3] ASTRON, the Netherlands Institute for Radio Astronomy, Postbus 2, 7990 AA Dwingeloo, The Netherlands
[4] Centre for Astrophysics Research, School of Physics, Astronomy and Mathematics, University of Hertfordshire, College Lane, Hatfield AL10 9AB, UK
[5] International Centre for Radio Astronomy Research – Curtin University, GPO Box U1987, Perth, WA 6845, Australia
[6] GEPI & USN, Observatoire de Paris, Université PSL, CNRS, 5 Place Jules Janssen, 92190 Meudon, France
[7] Department of Physics & Electronics, Rhodes University, PO Box 94, Grahamstown, 6140, South Africa
[8] Fakultät für Physik, Universität Bielefeld, Postfach 100131, 33501 Bielefeld, Germany
[9] SUPA, Institute for Astronomy, Royal Observatory, Blackford Hill, Edinburgh, EH9 3HJ, UK
[10] Italian ALMA Regional Centre, Via Gobetti 101, 40129, Bologna, Italy
[11] INAF-Osservatorio Astronomico di Padova, Vicolo dell'Osservatorio 5, 35122 Padova, Italy
[12] Astrophysics, Department of Physics, Keble Road, Oxford, OX1 3RH, UK
[13] University of the Western Cape, Private Bag X17, Bellville, Cape Town 7535, South Africa
[14] Thüringer Landessternwarte, Sternwarte 5, 07778 Tautenburg, Germany
[15] STFC UK Astronomy Technology Centre, Royal Observatory, Blackford Hill, Edinburgh, EH9 3HJ, UK
[16] Astrophysics & Cosmology Research Unit, School of Mathematics, Statistics & Computer Science, University of KwaZulu-Natal, Durban 3690, South Africa

Received 26 November 2020 / Accepted 24 January 2021

ABSTRACT

With the advent of new generation low-frequency telescopes, such as the LOw Frequency ARray (LOFAR), and improved calibration techniques, we have now started to unveil the subgigahertz radio sky with unprecedented depth and sensitivity. The LOFAR Two Meter Sky Survey (LoTSS) is an ongoing project in which the whole northern radio sky will be observed at 150 MHz with a sensitivity better than 100 μJy beam^{-1} at a resolution of 6″. Additionally, deeper observations are planned to cover smaller areas with higher sensitivity. The Lockman Hole, the Boötes, and the Elais-N1 regions are among the most well known northern extra-galactic fields and the deepest of the LoTSS Deep Fields so far. We exploited these deep observations to derive the deepest radio source counts at 150 MHz to date. Our counts are in broad agreement with those from the literature and show the well known upturn at $\leq$1 mJy, mainly associated with the emergence of the star-forming galaxy population. More interestingly, our counts show, for the first time a very pronounced drop around $S \sim 2$ mJy, which results in a prominent "bump" at sub-mJy flux densities. Such a feature was not observed in previous counts' determinations (neither at 150 MHz nor at a higher frequency). While sample variance can play a role in explaining the observed discrepancies, we believe this is mostly the result of a careful analysis aimed at deblending confused sources and removing spurious sources and artifacts from the radio catalogs. This "drop and bump" feature cannot be reproduced by any of the existing state-of-the-art evolutionary models, and it appears to be associated with a deficiency of active galactic nuclei (AGN) at an intermediate redshift ($1 < z < 2$) and an excess of low-redshift ($z < 1$) galaxies and/or AGN.

Key words. galaxies: evolution – surveys – radio continuum: general

1. Introduction

Large-area radio surveys are very important for statistical studies of radio source populations, addressing astrophysical properties and cosmological evolution of radio galaxies, quasars, and starburst galaxies. In the past, several wide-area radio surveys were carried out at low radio frequencies, such as the Cambridge Surveys (3C, 4C, 6C, and 7C at around 160 MHz: Edge et al. 1959; Bennett 1962; Pilkington & Scott 1965; Gower et al. 1967; Baldwin et al. 1985). However, the calibration of low-frequency radio data is challenging due to the direction-dependent, time-varying effects of the ionosphere that affects both the amplitude and the phase of the radio signal. Since these effects are only prominent in the megahertz (MHz) regime, the focus of wide-area and all-sky radio surveys switched to around 1 GHz in the last decades, resulting in the NRAO VLA Sky Survey (NVSS:

Condon et al. 1998), the Sydney University Molonglo Sky Survey (SUMSS: Mauch et al. 2003), and the Faint Images of the Radio Sky at Twenty-Centimeters (FIRST) survey (Becker et al. 1995; White et al. 1997).

The higher sensitivity and higher spatial resolution of surveys at gigahertz (GHz) frequencies also allowed us to probe deeper and deeper flux densities, and today we have several deep surveys covering degree-scale fields, which are sensitive to the sub-mJy and μJy radio populations (see e.g., Prandoni et al. 2000a,b, 2006, 2018; Hopkins et al. 2003; Schinnerer et al. 2004, 2007; Hales et al. 2014a; Smolčić et al. 2017). After many years of studies, it is now well established that the sub-mJy radio population has a composite nature. Radio-loud (RL) active galactic nuclei (AGN) are dominant down to 1.4 GHz flux densities of 200–300 μJy, and star-forming galaxies (SFGs) become dominant below about 100–200 μJy (Smolčić et al. 2008; Bonzini et al. 2013; Prandoni et al. 2018; Bonato et al. 2021). A significant fraction of the sources below 100 μJy can also show signatures of AGN activity in the host galaxy at other bands (IR, optical, X-ray), but they rarely display the large-scale radio jets and lobes typical of classical radio galaxies. Most of them are unresolved or barely resolved on a few arcsec scale, that is to say on scales similar to the host galaxy size. The origin of the radio emission in these, so-called radio-quiet, AGN is debated: it may come from star formation in the host galaxy (Padovani et al. 2011, 2015, Bonzini et al. 2013, 2015; Ocran et al. 2017; Bonato et al. 2017) or from low-level nuclear activity (White et al. 2015, 2017; Maini et al. 2016; Herrera Ruiz et al. 2016, 2017; Hartley et al. 2019). Most likely, such AGN are composite systems where star formation and AGN-triggered radio emission coexist over a wide range of relative contributions (e.g., Delvecchio et al. 2017). This scenario is also supported by the modeling work of Mancuso et al. (2017, see also Macfarlane et al., in prep.).

Being sensitive to SFGs up to the epoch of the peak of their activity ($z \sim 2$–3) and reaching the dominant radio-quiet (RQ) AGN population for the first time, deep radio surveys probing the μJy regime can be used as a very important dust and gas-obscuration-free tool to study both AGN activity and star formation and how they evolve with cosmic time. However, to overcome uncertainties introduced by low statistics, cosmic variance effects (Heywood et al. 2013), and other systematics (Condon et al. 2012), deep-radio surveys that cover wide areas ($\gg$1 deg^2) and have multiband ancillary data are needed. Such wide–area surveys are also useful to investigate the role of the environment in driving the growth of galaxies and supermassive black hole (SMBH), and to better trace rare radio source populations.

With the advent of a new generation of low-frequency telescopes and better data processing techniques we can now revisit the radio sky at low-frequency. With the Murchison Widefield Array (MWA; Lonsdale et al. 2009), Wayth et al. (2015) have carried out the GaLactic and Extragalactic All-sky MWA survey (GLEAM; Hurley-Walker et al. 2017), reaching a sensitivity of a few mJy beam^{-1} at a resolution of a few arcminutes. The GMRT has significantly improved the low-frequency view of the radio sky in terms of sensitivity and angular resolution. This has already been shown in a few low-frequency surveys centered around 150 MHz (e.g., Ishwara-Chandra et al. 2010, Sirothia et al. 2009, Intema et al. 2011, 2017).

The Low Frequency Array (LOFAR; van Haarlem et al. 2013a) is one of the key pathfinders to the Square Kilometre Array (SKA). Most of the LOFAR antennas are based in the Netherlands, with baseline lengths ranging from 100 m to 120 km. Additional remote stations are located throughout various countries in Europe. The longest baseline of LOFAR can provide a resolution of 0.3″ at 150 MHz. The combination of LOFAR's large field of view, wide range of baseline lengths, and large fractional bandwidth makes it a powerful instrument for performing large area and deep sky surveys. The LOFAR Two Meter Sky Survey (LoTSS) is an an ongoing project in which the whole northern sky is observed with a sensitivity better than 100 μJy beam^{-1} at the resolution of 6″ allowed by the Dutch LOFAR stations. The first data release (DR1) is described by Shimwell et al. (2017, 2019). The LoTSS also includes deeper observations of a number of preselected regions, where the aim is to eventually reach an rms depth of 10 μJy beam^{-1} at 150 MHz (Röttgering et al. 2011). In order to scientifically exploit these more sensitive surveys (collectively known as LoTSS Deep Fields), complementary multiwavelength data are necessary, most notably to identify the host galaxies of the extra-galactic radio sources and determine their redshift. For this reason observations were focused on fields with the highest quality multiwavelength data available. The Lockman Hole, the Boötes, and the European Large-Area ISO Survey-North 1 (ELAIS-N1) fields are the deepest of the LoTSS Deep Fields so far (see Tasse et al. 2021; Sabater et al. 2021; respectively Papers I and II of this series). All have rich multiwavelength ancillary data, covering a broad range of the electromagnetic spectrum, from X-ray to radio bands.

The Lockman Hole (LH hereafter) is one of the best studied extragalactic regions of the sky. It is characterized by a very low column density of Galactic HI (Lockman et al. 1986) making it an ideal field to study extragalactic sources with deep observations in the mid-IR, FIR, and submillimeter (Lonsdale et al. 2003; Mauduit et al. 2012; Oliver et al. 2012), optical/NIR (Muzzin et al. 2009; Fotopoulou et al. 2012; Hildebrandt et al. 2016), and X-ray (Polletta et al. 2006; Brunner et al. 2008). A variety of radio surveys cover limited areas within the LH region, at several frequencies. The widest deep radio survey so far consists of a 6.6 deg^2. 1.4 GHz mosaic obtained with the Westerbork (WSRT) telescope (1σ sensitivity $\sim$10 μJy beam^{-1}; Prandoni et al. 2018). We refer to Prandoni et al. (2018) for a comprehensive summary of the available multifrequency and multiband coverage in this region (see also Kondapally et al. 2021, Paper III of this series).

The Boötes (Boo hereafter) field was originally targeted as part of the NOAO Deep Wide Field Surveys (NDWFS; Jannuzi & Dey 1999) which covers $\sim$9 deg^2 in the optical and near infrared (K) bands. Ancillary data is available for this field including X-ray (Murray et al. 2005; Kenter et al. 2005), UV (GALEX; Martin et al. 2003), and mid-infrared (Eisenhardt et al. 2004). Radio observations have also been carried out at 153 MHz with the GMRT (Intema et al. 2011; Williams et al. 2013), at 325 MHz with the VLA (Croft et al. 2008; Coppejans et al. 2015) and at 1.4 GHz with the WSRT (de Vries et al. 2002).

The Elais-N1 (EN1 hereafter) field has deep multiwavelength (0.15–250 μm) data taken as part of many different surveys – optical: the Panoramic Survey Telescope and Rapid Response System; Pan-STARRS (Chambers et al. 2016) and Hyper-Suprime-Cam Subaru Strategic Program (HSC-SSP) survey, u-band: *Spitzer* Adaptation of the Red-sequence Cluster Survey; SpARCS: Muzzin et al. 2009, UV: Deep Imaging Survey (DIS): Martin et al. 2005, NIR J and K band: the UKIDSS Deep Extragalactic Survey (DXS) DR10 (Lawrence et al. 2007), MIR: IRAC instrument on board the *Spitzer* Space Telescope: SWIRE; Lonsdale et al. 2003 and The *Spitzer* Extragalactic Representative Volume Survey (SERVS; Mauduit et al. 2012).

Mahony et al. (2016) presented the first LOFAR 150 MHz map of the LH with a sensitivity of 160 μJy beam^{-1} at a

Table 1. Overview of the statistical properties of the three LoTSS Deep Fields.

Field	RA (hh:mm:ss)	Dec (dd:mm:ss)	Obs. time (hr)	σ_c (μJy beam^{-1})	Area^{full} (deg^2)	N_S^{raw}	σ_{med}^{full} (μJy beam^{-1})	Area^{masked} (deg^2)	N_S^{final}	σ_{med}^{masked} (μJy beam^{-1})
LH	10:47:00.0	+58:04:59.0	112	22	25.0	50 112	42	10.3	31 162	31
Boo	14:32:00.0	+34:30:00.0	80	32	26.5	36 767	60	8.6	19 179	44
EN1	16:11:00.0	+55:00:00.0	164	17	24.3	69 954	33	6.7	31 610	23

Notes. The columns are as follows: pointing center (RA and Dec); total observing time; RMS noise reached at the center of the image (σ_c); area covered by the raw catalog (Area^{full}), number of sources in the raw catalog (N_S^{raw}) and median RMS noise in the area covered by the raw catalog (σ_{med}^{full}); same parameters for the final catalog (Area^{masked}, N_S^{final}, σ_{med}^{masked}).

resolution of $18.7'' \times 16.4''$. Williams et al. (2016) presented the first LOFAR map of the Boo field at a resolution of $5.6'' \times 7.4''$ with an rms of 120 μJy beam^{-1}. A deeper image of the Boo field, reaching an rms of 55 μJy at its center, was presented by Retana-Montenegro et al. (2018). Tasse et al. (2021; Paper I) present the deepest, high-resolution ($6''$) low-frequency images and catalogs of the LH and Boo fields at 150 MHz and also describe the general method followed for the data reduction of the LoTSS Deep Fields. The even deeper LOFAR observations of the EN1 field are presented separately by Sabater et al. (2021; Paper II).

One of the immediate science products of deep radio surveys is the determination of the radio source counts, which can provide useful comparison with counts predictions based on evolutionary models of radio source populations. In the present paper, we collectively exploit the LH, Boo and EN1 deep LOFAR data to derive the deepest radio source counts at 150 MHz ever. The derived source counts are compared with other existing determinations, as well as with state-of-the-art radio source evolutionary models (e.g., Wilman et al. 2008; Mancuso et al. 2017; Bonaldi et al. 2019).

The outline of the paper is as follows. In Sect. 2 the data reduction and the imaging process followed to obtain the deep images of the LH, Boo and EN1 are described in brief. In Sect. 3, we summarize the source extraction process and we describe the derived source catalogs and corresponding properties. This is followed by an analysis of the source size distribution and of the catalog incompleteness due to resolution bias (Sect. 4). Eddington bias and related incompleteness are discussed in Sect. 5. Section 6 presents the derived 150 MHz source counts and their comparison with state-of-the-art evolutionary models. We summarize our results in Sect. 7. Throughout this paper, we have used the convention $S_\nu \propto \nu^\alpha$.

2. Observations and data reduction

The observations and data reduction of the LoTSS Deep Fields are described in detail in Paper I, but for completeness we provide a brief summary. Each of the deep fields was observed using the LOFAR High Band Antenna (HBA) in its `HBA_DUAL_INNER` mode. Observations were taken in approximately 8hr blocks and the total integration times were 112, 80 and 164 h for the LH, Boo and EN1 fields respectively[1]. The phase centers of the three pointings are listed in Table 1 (RA, Dec). The calibration of the data was completed in two steps. Firstly a direction-independent calibration was performed using the PREFACTOR pipeline[2] which is described in van Weeren et al. (2016) and Williams et al. (2016) and corrects for direction independent effects (see de Gasperin et al. 2019). To efficiently deal with the large data rates, this pipeline is run on a compute cluster connected to the LOFAR archive (see Mechev et al. 2018 and Drabent et al. 2019). The resulting data products are then calibrated with the latest version of DDF-PIPELINE[3] which is briefly outlined in Sect. 5.1 of Shimwell et al. (2019) and detailed by Paper I. This pipeline is based on the kMS solver (Tasse 2014; Smirnov & Tasse 2015) and the DDFacet imager (Tasse et al. 2018) to calibrate for direction-dependent effects, such as ionosphere-induced and beam model errors, and apply these solutions whilst imaging.

As described in Tasse et al. (2018), for each deep field a single good observation is selected and run through DDF-PIPELINE. The resulting sky model, together with all observations from that particular field, are then input into a second run of DDF-PIPELINE which calibrates all the data off that sky model, before imaging all the data together and completing a final round of direction independent and direction-dependent self-calibration. The frequency coverage used to produce the images is 120–168 MHz for Boo and LH and 115–177 MHz for EN1[4].

As described in Papers I and II, the peak and integrated flux densities of the final images were rescaled by factors of 0.920, 0.859 and 0.796 for the LH, Boo and EN1 fields respectively. These scaling factors were derived from the comparison of the LOFAR flux densities with a variety of shallower radio surveys available at various frequencies over these fields. The minimum sensitivity reached at the center of the images (after rescaling) is $\sigma_c \sim 22, 32, 20$ μJy beam^{-1}, respectively, at a resolution of $6''$ (see Table 1). Although dynamic range effects are present around bright sources, in all cases the final image noise levels are within $\sim$10% of the noise levels predicted from 8-h depths, assuming an rms scaling with time $t^{-0.5}$. We note that the noise measured in the Boo field is higher compared to the other two, also due to its lower declination.

3. Source extraction, masking and deblending

Initial source catalogs were extracted in each field using the PYthon Blob Detector and Source Finder (PyBDSF; Mohan & Rafferty 2015). The strategy followed for LH and Boo is detailed in Paper I. In brief, the source detection threshold was set at 5σ for the peak flux density and at 3σ for the definition of the contiguous pixels used for the source Gaussian fitting, where σ is defined as the local rms noise at the source position. To measure the background noise variations across the images, a sliding

[1] A full overview of the observation details is given in Table 1 of Paper I (for the LH and the Boo fields) and in Table 1 of Paper II (for the EN1 field).
[2] https://github.com/lofar-astron/prefactor
[3] https://github.com/mhardcastle/ddf-pipeline
[4] The exact central frequency of the imaged band is therefore 144 MHz for LH and Boo, and 146 MHz for EN1.

box of the size of 40×40 synthesized beams was used. For high signal-to-noise ($\geq$150) sources, the box size was reduced to 15×15 synthesized beams in order to capture the increased local noise level more accurately. For EN1 a slightly different set of parameters was used (see Table C.1 of Paper II). The PyBDSF wavelet decomposition mode was used in all fields to better describe complex sources characterized by very extended emission. PyBDSF produces source catalogs, by grouping together Gaussian components that belong to the same island of emission. A flag is assigned to each source according to the number of Gaussian components fitted and grouped together to form a source: 'S' and 'M' refer to sources fitted by a single and multiple Gaussian components respectively, whereas 'C' means that the source lies within the same island as another source. For a more detailed description of the method and format of the catalogs, see the webpage[5] and Shimwell et al. (2019). The catalogs were cut at a distance from the pointing center roughly corresponding to 0.3 of the 150 MHz LOFAR primary beam power (corresponding to fields of view of about 25 deg^2). The footprints of these initial PyBDSF catalogs (hereafter referred to as raw catalogs) are shown in light colors in Fig. 1. The total number of sources over these footprints is respectively 50, 112 (LH), 36, 767 (Boo) and 69, 954 (EN1).

Deep and wide optical and IR data are available for part of the LoTSS Deep Fields. Over these subregions, we were able to carry out a further process of multiwavelength cross-matching and source characterization (see Paper II). This process, based on a combination of statistical methods and visual classification schemes, allowed us to identify the host galaxies of over 97% of the detected radio sources[6]. In addition it allowed us to produce a cleaner and more reliable radio source catalog by (a) removing spurious detections (mainly artifacts introduced by residual phase errors around bright radio sources), and (b) mitigating PyBDSF failures in correctly associating components to a source. Incorrect associations can occur in two main ways. Firstly, radio emission from physically distinct nearby sources could be associated as one PyBDSF source (blended sources). Such blends are more common at the faint end of the radio catalogs, where the source density is higher. Secondly, sources with multiple components could be incorrectly grouped into separate PyBDSF sources due to a lack of contiguous emission between the components. For example, this can occur for sources with well separated double radio lobes.

An extensive description of the aforementioned process is given by Paper II (see also Williams et al. 2019). Here we only provide a brief summary. All sources were evaluated through a decision tree to select those that require direct visual inspection and those that can be cross-matched through a Likelihood Ratio (LR) analysis. Sources with secure radio positions (f.i. those described by compact single Gaussian components) were selected as suitable for the LR method. Very extended, complex or multiple Gaussian sources were classified through visual inspection froma group consensus, as well as sources that turn out to have an unreliable LR identification. Artifacts are generally found among sources with no reliable identification. Blended sources are typically recognized by the fact that (at least some of) their Gaussian components have very reliable distinct identifications. When confirmed through visual inspection, they are deblended.

After this cleaning process, the radio catalogs collect respectively 31, 163 (LH), 19, 179 (Boo) and 31, 645 (EN1) sources, distributed respectively over 10.3 deg^2 (LH), 8.6 deg^2 (Boo) and 6.7 deg^2 (EN1). In the following we refer to these deblended and associated catalogs as final catalogs. The footprints of the final catalogs are shown in dark colors in Fig. 1. The irregular shape of these footprints follows the optical/IR sky coverage, corresponding to the region where source association and cross-identification is performed. We note that 'holes' are present in such footprints, due to the fact that regions with optically bright

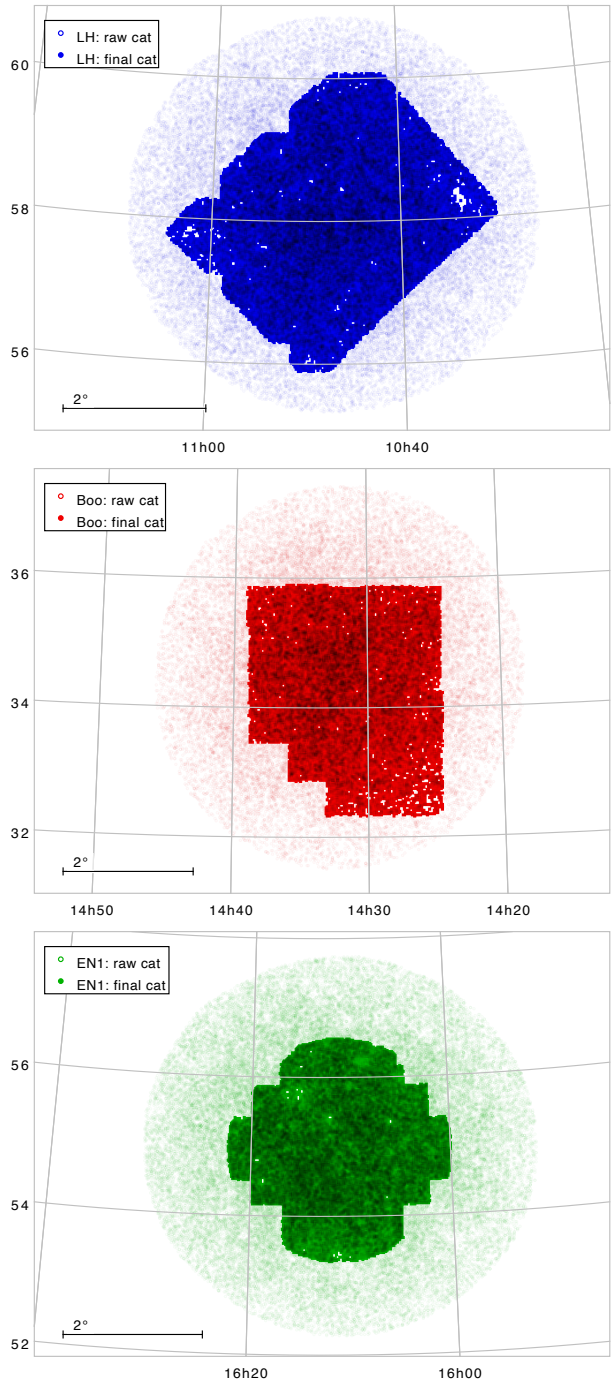

Fig. 1. LH (*top*), Boo (*middle*) and EN1 (*bottom*) fields targeted by LOFAR at 150 MHz. Light colors refer to the raw catalogs, cut at a distance from the pointing center of 0.3 of the LOFAR 150 MHz primary beam power. Darker colors refer to the final catalogs. The varying shape of their footprints highlights the regions with available optical/IR data. The areas of the optical/IR footprints are listed in Table 1.

[5] http://www.astron.nl/citt/pybdsf/
[6] 97.6% for EN1 and LH; 96.9% for Boo.

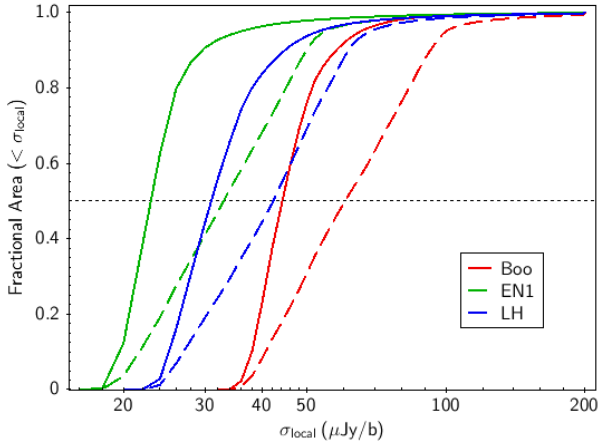

Fig. 2. Visibility functions of the raw (dashed lines) and final (solid lines) catalogs presented in this paper. Blue, red and green colors correspond to the LH, Boo and EN1 fields, respectively. The visibility functions represent the cumulative fraction of the total area of the noise map characterized by a noise lower than a given value. We caution that the total area covered by the final catalogs is much smaller than the one covered by the raw catalogs (see Table 1).

stars (which typically produce artifacts in their surroundings) were masked.

In addition we have generated pixel-matched images in each waveband and extracted forced aperture-matched photometry from ultraviolet to infrared wavelength (Paper II), deriving high-quality photometric redshifts for around 5 million objects across the three fields (see Duncan et al. 2021, Paper IV, for more details). The raw and final radio catalogs, as well as the optical/IR and photometric catalogs, are available on the LOFAR Surveys Data Release site web-page[7].

3.1. Visibility function of raw and final catalogs

Figure 2 shows the so-called visibility function (i.e., the cumulative fraction of the total area of the noise map characterized by noise measurements lower than a given value) for the LH (blue), Boo (red) and EN1 (green) fields. Raw and final catalogs are indicated respectively by the dashed and solid lines. We note that the visibility functions of final catalogs are significantly steeper than those of the raw catalogs. This is due to the fact that the final catalogs are mostly confined in the inner, most sensitive parts of the LOFAR fields. As a consequence the median noise is significantly lower for final than for raw catalogs (see Table 1).

3.2. Source size deconvolution

The characterization of resolved versus unresolved sources in our catalogs is important in order to correct the catalogs for the incompleteness introduced by so-called "resolution bias" (described in Sect. 4). The total flux density ($S_{\rm total}$) of a source can be written as:

$$S_{\rm total}/S_{\rm peak} = \theta_{\rm maj}\theta_{\rm min}/b_{\rm min}b_{\rm maj} \quad (1)$$

where $S_{\rm peak}$ is the source peak flux density, $\theta_{\rm min}$ and $\theta_{\rm maj}$ are the source full-width-half-maximum (FWHM) axes, and $b_{\rm min}$ and $b_{\rm maj}$ are the restoring beam FWHM axes. In an ideal image, in the absence of noise, the total flux density of a point source is equal to its peak flux density. In real images both the total and peak flux density measurements of point sources are affected by errors. This means that not all sources with $S_{\rm total} > S_{\rm peak}$ would be genuinely resolved sources. The $S_{\rm total}/S_{\rm peak}$ ratio as a function of signal-to-noise ratio ($S/N = S_{\rm peak}/\sigma$, where σ is the local rms noise), can be used to establish a statistical criterion to establish if a source is likely extended or point-like (see e.g., Prandoni et al. 2000b, 2006). In Fig. 3, the ratio of the total to peak flux

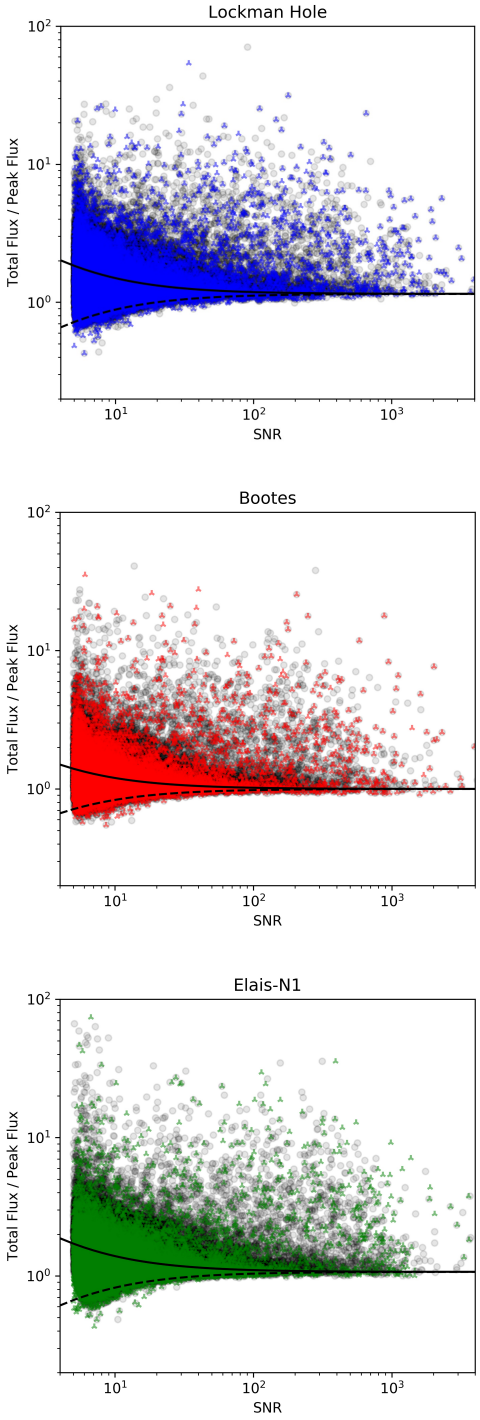

Fig. 3. Total to peak flux density ratio as a function of signal to noise ratio ($S/N = S_{\rm peak}/\sigma$) for both the raw (black transparent circles) and final ($\curlywedge$ symbols in blue, red and green colors) catalogs in the LH, Boo and EN1 fields (respectively *from top to bottom panels*). The dashed and solid lines represent the unresolved source distribution lower and upper envelopes respectively (see text for more details).

[7] https://lofar-surveys.org/releases.html

Table 2. Parameters describing the unresolved/resolved sources' dividing lines (see Eqs. (2) and (3)) for the LH, Boo and EN1 catalogs.

Field	A	B	$\%_{\rm resolved}$	
			Raw	Final
LH	1.15	3.0	34	25
Boo	1.00	2.0	47	38
EN1	1.07	3.0	35	24

densities is shown as a function of S/N for both raw and final catalogs. A lower envelope of the source distribution can be defined by the following equation:

$$S_{\rm total}/S_{\rm peak} = {\rm A}/(1 + {\rm B}/(S/N)), \quad (2)$$

where A and B are two free parameters (see dashed lines in each panel of Fig. 3). As expected, going to higher S/N, measurement errors get smaller. At $S/N \gg 100$ the 2nd term of Eq. (2) can be neglected, and the $S_{\rm total}/S_{\rm peak}$ tends to A. In an ideal case, where radial smearing is taken care of, the ratio of the total over the peak flux density for point sources should converge to a value of $A = 1$ at very high S/N. The DDFacet pipeline implements a facet dependent PSF which, for deconvolved sources, accounts for the impact of time and bandwidth smearing (Tasse 2014). However, due to imperfect calibration of the PSF across the field and/or smearing of sources due to ionospheric distortions, the value of the ratio at high signal-to-noise sources can be found to be higher than 1 and can be field-dependent (as ionospheric effects are time and spatially dependent). The values of A for the LH, Boo and EN1 field are respectively 1.15, 1.00 and 1.07 (see Table 2). This could potentially mean that the Boo field is less affected by ionospheric smearing when compared with LH and EN1. The B value also changes depending on the field, with Boo showing a lower value than LH and EN1 (see Table 2), again indicating smaller errors in the determination of source flux densities. We notice that the parameters given in Table 2 provides a good description of both raw and final catalogs. The lower envelopes can then be mirrored around the $S_{\rm total}/S_{\rm peak} = {\rm A}$ axis to get the upper envelopes:

$$S_{\rm total}/S_{\rm peak} = {\rm A} \cdot (1 + {\rm B}/(S/N)). \quad (3)$$

Sources lying above the upper envelopes (dashed black lines in each panel) are then considered to be truly extended or resolved sources. Sources below the upper envelopes are considered to be point sources. The fraction of resolved sources in each field is given in Table 2. In final catalogs the fraction of resolved sources vary from 24–25% (EN1 and LH) to 38% (Boo). The ∼10% higher fractions observed in raw catalogs reflect the larger number of bright extended sources detected in their larger FoV. These fractions should be considered as indicative, as they depend on the criteria used to define them. Sabater et al. (2021), for instance, as part of their detailed analysis of the EN1 field, used more stringent criteria, which also include additional sources of errors for the source flux densities, and estimated that between 4 and 11% of the sources in the EN1 raw catalogs are genuinely extended (see Paper II for more details). Nevertheless, we decided to apply the same approach to all fields, and to both final and raw catalogs, to enable a consistent statistical analysis of the source size distribution in the three fields (see Sect. 4).

4. Source size distribution and resolution bias

In deriving the source counts, the completeness of the catalogs in terms of total flux density needs to be estimated. Such completeness depends on source angular sizes, since, as shown by Eq. (1), a larger source of a given total flux density will drop below the 5σ limit of a survey more easily than a smaller source of the same total flux density. This effect, called resolution bias, results from the fact that the detection of a source depends on its peak flux density. Following Prandoni et al. (2001, 2006), we can use Eq. (1) to calculate the approximate maximum deconvolved size ($\Theta_{\rm max}$) a source of a given total flux density, $S_{\rm total}$, can have before dropping below the 5σ limit of the catalog:

$$\Theta_{\rm max} = \Theta_N \sqrt{(S_{\rm total}/(5\sigma) - 1} \quad (4)$$

where $\Theta_{\rm N} \equiv \sqrt{b_{\rm maj} b_{\rm min}}$ is the geometric mean of the restoring beam axes. In our case $\Theta_{\rm N} = b_{\rm maj} = b_{\rm min} = 6''$.

In Fig. 4 we show the deconvolved source sizes as a function of the total flux density for both raw and final catalogs. Each panel corresponds to a different field: LH (top-left), Boo (top-right) and EN1 (bottom). Deconvolved sizes are defined as the geometric mean of the major and minor FWHM axes, except for well resolved radio galaxies, which are better described by their major axis. Deconvolved sizes of point sources are set to zero. As expected, the upper envelope of the source size distributions approximately follow the $\Theta_{\rm max} - S_{\rm total}$ relation (short-long-dashed line) in all fields.

Equations (1) and (3) can also be used to derive an approximate minimum intrinsic angular size ($\Theta_{\rm min}$) that can be resolved reliably as a function of the source peak flux density:

$$\Theta_{\rm min} = \Theta_{\rm N} \sqrt{{\rm A} \cdot (1 + {\rm B}/(S/N)) - 1}\,. \quad (5)$$

The curve representing $\Theta_{\rm min}$ is shown in Fig. 4 by the solid lines.

In order to quantify the fraction of sources larger than $\Theta_{\rm max}$, and in turn the incompleteness affecting our catalog, we need to know the true intrinsic radio source size distribution within the flux density range probed by our survey. We start assuming the empirical integral distribution proposed by Windhorst et al. (1990) for 1.4 GHz-selected samples:

$$h(>\Theta) = \exp[-\ln 2\,(\Theta/\Theta_{\rm med})^q] \quad (6)$$

where $q = 0.62$ and the median source size varies with the total flux density as follows:

$$\Theta_{\rm med} = k \times (S_{\rm 1.4GHz})^m \quad (7)$$

with $k = 2''$, $m = 0.3$, $S_{\rm 1.4GHz}$ expressed in mJy. The Windhorst et al. (1990) relations are extensively used in the literature to estimate the resolution bias, either for 1.4 GHz selected samples (see e.g., Prandoni et al. 2001, 2018; Huynh et al. 2005; Hales et al. 2014a), or for surveys at other frequencies, including LOFAR HBA ones (Mahony et al. 2016; Williams et al. 2016; Retana-Montenegro et al. 2018). We converted the median size – flux density relation to 150 MHz assuming a spectral index $\alpha = -0.7$. This assumption is appropriate for radio catalogs dominated by faint sub-mJy radio sources. Indeed spectral index analyses performed using shallower ($S_{\rm 150\,MHz} \gtrsim 1$ mJy) LOFAR observations of the Boötes and LH fields, report overall median spectral index values of $\alpha^{\rm 1.4\,GHz}_{\rm 150\,MHz} = -0.73 \pm 0.33$ and -0.78 ± 0.24, for AGN and star-forming galaxies respectively (Boötes; Calistro Rivera et al. 2017), as well as a flattening of the spectral index going to lower flux densities, with a median value